# Supporting Information for "Dynamic full-field imaging of rupture radiation: Material contrast governs source mechanism"

Aichele J.[1,2] *, Latour S.[3], Roux P. [2]and Catheline S.[1]

[1]Laboratory of Therapeutic Applications of Ultrasound, INSERM & University of Lyon, Lyon, France

[2]ISTerre, Univ. Grenoble Alpes, Univ. Savoie Mont Blanc, CNRS, IRD, Univ. Gustave Eiffel, Grenoble, France

[3]Institute of Astrophysics and Planetology, IRAP & University of Toulouse III, Toulouse, France

## Contents of this file



## Additional Supporting Information (Files uploaded separately)

---

*currently at Department of Earth Sciences, Institute of Geophysics, Swiss Federal Institute of Technology, Zürich, Switzerland

1. Wave propagation video of the strong interface experiment. Contains the whole two second long acquisition.

2. Wave propagation video of the weak interface experiment. Contains the whole two second long acquisition.

3. Caption for video S1

4. Captions for video S2

## 1. Introduction

Section 2 contains a detailed description of the experimental setup, experimental workflow and the imaging methodology used to acquire the data presented in the main article, supplemented by Table S1. A detailed description of the analytic simulations, including the governing Green's functions are given as well. The simulation source parameters are visualized by means of additional plots Figs. S10 to S14. Supporting data is given in Section 4 and the two supplementary videos. The two videos show the particle velocities acquired throughout the entire experiments, from which all figures showing experimental results in the main article are derived. All additional figures showing experimental results are also derived from these two datasets of the strong and weak bimaterial experiment.

## 2. Detailed Materials & Methods

### 2.1. Samples

We use homemade polyvinyl-alcohol (PVA) hydrogels. These gels are commonly used to mimic biological tissue. In comparison with gelatin and agar-gels they have the advantage of a much longer lifetime if stored in water. The production process consist of the following consecutive steps:

- Solution of PVA-powder in hot water under constant stirring.
- Addition of 0.1-0.5 % of graphite powder to introduce the scatterers that assure the ultrasonic speckle.
- Rapid cool-down in an ice-bath of the viscous solution until gelification sets in.
- Freezing at $-18\,^{\circ}\mathrm{C}$ until complete gelification is reached.
- Complete thawing of the gel.

The last two steps are repeated until the gel has the desired elasticity. It should be noted, that the homemade gels are not homogeneous. During the production of the large samples required for the setup, incomplete solution of the PVA-powder could not be avoided and the long time needed for complete solidification led to deposition of graphite and PVA-powder at the bottom of the gel.

### 2.2. Friction bench

The motor is a Kollmorgen® AKM™ stepper motor, depicted in Fig. S1. It is piloted through a LabVIEW (National Instruments, Austin, TX, USA) interface which ensures synchronization with the imaging device. The motor drives an endless screw, which in turn drives a glass plate through a wagon that is sliding on low-resistance bills on two rails. The motor controls the

rotation rate of the screw and thus the driving speed of the wagon. The movement of the glass plate and the friction of the asperity lead to deformation of a hydrogel, which is hold in a fixed position on the friction bench.

### 2.3. Asperity

We focus on a spatially limited sand asperity that gives rise to granular friction. A small patch of fine to medium sand (<0.5 mm), is placed on the glass plate in the center of the hydrogel position. The sand is not completely dry, because PVA hydrogels loose water, especially under stress. This becomes evident in the cohesion of sand grains after the experiment.

### 2.4. Imaging device

The imaging probe is a 128-element L7-4 (Philips) ultrasound probe centered at 5 MHz. The probe is connected to a high-frame rate ultrasound scanner (Verasonics Vantage™) which works at up to 10 000 frames per second. The host computer ensures sequence programming as well as registration and treatment of the acquired data through a Matlab™ interface. Each ultrasound frame is obtained through emission of plane waves as in Sandrin, Catheline, Tanter, Hennequin, and Fink (1999) and beamforming of the backscattered signals.

### 2.5. Imaging method

In order to visualize the wave propagation, we apply phase-based motion estimation on subsequent beamformed ultrasound frames (Pinton et al., 2005). Similar to ultrasound Doppler techniques, the retrieved US phase difference gives the relative shear wave displacement in the micrometer range.

This phase shift or phase difference can be expressed through the Fourier shift theorem. The theorem states, that a signal $x(t)$ delayed by $dt$ has a Fourier transform that equals the Fourier transform of $x(t)$ multiplied by $e^{-j\omega dt}$. Hence, $x(t-dt) \leftrightarrow e^{-j\omega dt}\hat{x}(\omega)$.

Because for beamformed ultrasound reflection images ($IQ$), only displacements in direction of the plane ultrasound wave can be recorded, the translation of the ultrasound reflection images is one-dimensional. The spatial coordinates along the axis of ultrasound propagation ($z$) are inferred from the ultrasonic travel-time and the central frequency of the probe. With a time difference $dt$ of snapshots $t_1$ and $t_2$ and US travel-time $\tau$ ($z \rightarrow \tau$) the theorem reads:

$$IQ(x,\tau,t_2) = IQ(x,\tau - d\tau,t_1) \tag{1}$$

$$\hat{IQ}_2(\xi,\omega,t_2) = e^{-j2\pi(\omega d\tau)}\hat{IQ}(\xi,\omega,t_1) \tag{2}$$

The phase shift $e^{-j2\pi(\xi d\tau)}$ is calculated by using the normalized cross power spectrum, which is retrieved through multiplication with the complex conjugate in the Fourier domain.

$$e^{-j2\pi(\omega d\tau)} = \frac{\hat{IQ}(\xi,\omega,t_1)\hat{IQ}^*(\xi,\omega,t_2)}{\left|\hat{IQ}(\xi,\omega,t_1)\hat{IQ}(\xi,\omega,t_2)\right|} \tag{3}$$

The argument of equation 3 gives thus the relative displacement between two images in radians and the particle velocity reads:

$$v_p(x,\tau) = \frac{c_0}{(4\pi f_c)}\arg(e^{-j2\pi(\omega d\tau)}) \tag{4}$$

- with $\tau$ being related to the spatial coordinate $z$ by $\lambda = \frac{c_0}{f_c}$ and $z$ being resolved by the imaging system at four points per US wavelength.

• with $c_0$ being the speed of ultrasound, approximately $1480\,\mathrm{m\,s^{-1}}$ (speed of sound in water) in soft matter, and $f_c$ being the central frequency of the probe.

In the IQ domain, the correlation is thus a simple point by point multiplication in the frequency domain and time-consuming windowing is not required. Due to the very high resolution of the probing ultrasound waves of $3\times10^{-5}\,\mathrm{m}$ and the high frame rate, the retrieved particle velocity can be locally integrated over time to get the total displacement along the ultrasound propagation direction. Furthermore, taking the spatial gradient of the accumulated displacement allows for estimation of one component of the strain tensor. Likewise, time differentiation leads to particle acceleration which is advantageous when continuous deformation masks simultaneous wave propagation.

### 2.6. Unidirectional shear force

The particle displacement in the direction $i$ inside a homogeneous body due to a unidirectional shear force in the direction $j$ is given by the convolution of the source time function $X_0(t)$ with the medium's Green's function $G_{ij}$:

$$\begin{aligned} u_i(\vec{x},t) &= X_0 * G_{ij} \\ &= \frac{1}{4\pi\rho}(3\gamma_i\gamma_j-\delta_{ij})\frac{1}{r^3}\int_{\frac{r}{a}}^{\frac{r}{b}} \tau X_0(t-\tau)d\tau \\ &+ \frac{1}{4\pi\rho\alpha^2}\gamma_i\gamma_j\frac{1}{r}X_0(t-\frac{r}{\alpha}) \\ &- \frac{1}{4\pi\rho}\beta^2(\gamma_i\gamma_j-\delta_{ij})\frac{1}{r}X_0(t-\frac{r}{\beta}), \end{aligned} \tag{5}$$

where $r$ is the distance from the source to the receiver, $\rho$ is density, $\alpha$ and $\beta$ are the compression and shear wave speeds, $\tau$ is the source time and $\delta_{ij}$ is the kronecker symbol. $\gamma_i$ is defined as $\gamma_i = \frac{x_i}{r}$. A thorough derivation is given in Chapter 3 and 4 of Aki and Richards (2009).

### 2.7. Double-couple point source

The displacement field induced by a shear dislocation can be described as a convolution of the seismic moment tensor with the Green's function. Using summation convention, the n-th displacement component is expressed as $u_n = M_{pq} * G_{np,q}$, with $M_0(t) = \mu\bar{u}(t)A$, where $\bar{u}$ is the averaged displacement discontinuity from the shear displacement, $A$ is fault area and $\mu$ is shear modulus. The time dependant point force function $X_0(t)$ for the unidirectional shear force has thus its equivalent for the DC in the material and slip area dependant displacement function $M_0(t)$. In polar coordinates with the DC location as origin, and vector form, the displacement due to a double-couple source reads:

$$\begin{aligned} u(\vec{x},t) = & \frac{1}{4\pi\rho}\vec{A}^N\frac{1}{r^4}\int_{\frac{r}{a}}^{\frac{r}{b}}\tau M_0(t-\tau)d\tau \\ & + \frac{1}{4\pi\rho\alpha^2}\vec{A}^{IP}\frac{1}{r^2}M_0(t-\frac{r}{\alpha}) + \frac{1}{4\pi\rho\beta^2}\vec{A}^{IS}\frac{1}{r^2}M_0(t-\frac{r}{\beta}) \\ & + \frac{1}{4\pi\rho\alpha^3}\vec{A}^{FP}\frac{1}{r}\dot{M}_0(t-\frac{r}{\alpha}) + \frac{1}{4\pi\rho\beta^3}\vec{A}^{FS}\frac{1}{r}\dot{M}_0(t-\frac{r}{\beta}), \end{aligned} \tag{6}$$

where the notation is equivalent to Eq. (5). The radiation patterns of the near field and the far and intermediate compression (P) and shear (S) field terms are described by:

$$\begin{aligned} \vec{A^N} = & \ 9\sin 2\theta\cos\phi\vec{\hat{r}} - 6(\cos 2\theta\cos\phi\vec{\hat{\theta}} - \cos\theta\sin\phi\vec{\hat{\phi}}) \\ \vec{A^{IP}} = & \ 4\sin 2\theta\cos\phi\vec{\hat{r}} - 2(\cos 2\theta\cos\phi\vec{\hat{\theta}} - \cos\theta\sin\phi\vec{\hat{\phi}}) \\ \vec{A^{IS}} = & -3\sin 2\theta\cos\phi\vec{\hat{r}} - 3(\cos 2\theta\cos\phi\vec{\hat{\theta}} - \cos\theta\sin\phi\vec{\hat{\phi}}) \\ \vec{A^{FP}} = & \ \sin 2\theta\cos\phi\vec{\hat{r}} \\ \vec{A^{FS}} = & \ \cos 2\theta\cos\phi\vec{\hat{\theta}} - \cos\theta\sin\phi\vec{\hat{\phi}}, \end{aligned}$$

where $\phi, \theta$ and $r$ are the spherical coordinates, with $\phi$ being the angle to the direction of the DC and $\theta$ being the angle to the orthogonal of the DC direction.

### 2.8. Kinematic simulations

The propagating ruptures are modeled by superposing unidirectional shear point forces or double-couple point forces in space and time. The same source function $X_0(t)$ or $M_0(t)$ is therefore shifted in x-direction and time according to the rupture speed profile. Along the prescribed rupture surface, each grid point, which is spaced at 0.3 mm acts thus as a point source, emitting at different times. We assume an axisymmetric setup and homogeneous medium and extract the wavefield in a $x - z$ plane for the simulation. As a consequence, the physical rupture surface of the experiment is reduced to a rupture line in the simulation. The only processing undertaken for visualization of the simulations is a median filter which was applied to the simulations in space in order to visually highlight the coherent wavefronts. This is due to the fact that the simulations were undertaken with an equivalent resolution in x and z while the experiment was acquired at a higher spatial resolution in z. Point source functions for the kinematic simulations and rupture speed profile resulting from the superposition of these point sources in time and space can be found in Figs. S10 to S14. The actual wavefield is retrieved by convolving the derivative with the Green's function and integrating the resulting wavefield to avoid non-smooth or long source functions in the computation. Note that the simulations are qualitative and the source amplitudes are normalized.

### 2.9. Wave and rupture speed measurements

Examples of the manual time of flight measurements from the strong bimaterial interface experiment are given in Figs. S15 and S16. The given uncertainty stems from the time resolution of the data acquisition. An example of the speed estimation from the supershear front, as described in the main article, is shown in Fig. S17.

## 3. Supplementary table

**Table S1.** Experimental parameters for the experiments presented in Fig. 2-5 (main article).

| **Experiment** Ref. | **Gel** Nr. | **PRF** $[\frac{frame}{s}]$ | **Drive speed** $[\frac{mm}{s}]$ | **Normal load** $[kg]$ | **Duration** [s] |
|---|---|---|---|---|---|
| Fig. 2-3 | Gel 1 | 3000 | 1 | $\approx 4.0$ | 2 |
| Fig. 4-5 | Gel 1+2 | 3000 | 2 | $\approx 2.5$ | 3 |

## 4. Supplementary figures

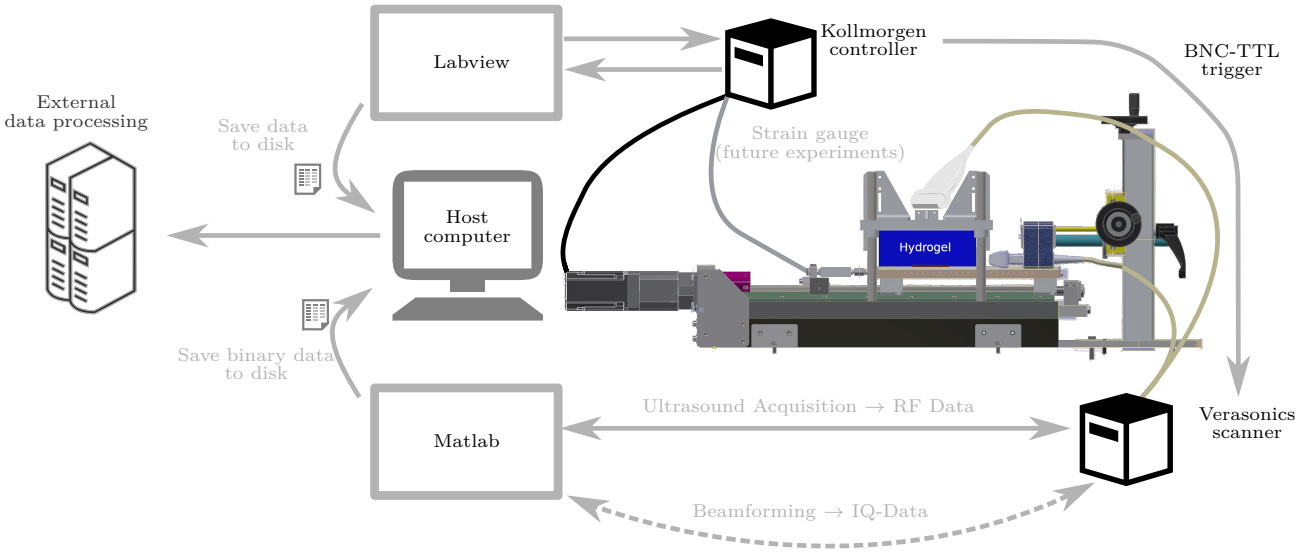


**Figure S1.** Experimental workflow: Raw-data acquisition, beamforming and post-processing are separate processes. This permits rapid succession of experiments. The length of the experiment is hereby only limited by the frame size of the raw data and the available memory of the host computer. Labview pilots the motor and triggers the ultrafast scanner via a BNC-TTL trigger. Center sketch: Friction bench. From left to right: A stepper motor drives an endless screw which displaces the wagon with the glass plate. A hydrogel is posed on the glass plate with a frictional layer of sand in between. Normal load is applied on top via weights. The gel is blocked in the direction of movement of the plate and a small part at the bottom is left free to deform. An ultrasound imaging probe is placed on the side or top of the gel with a layer of echography gel in-between to ensure coupling and omit stress induced by the probe. In this paper only the vertical probe position is investigated.

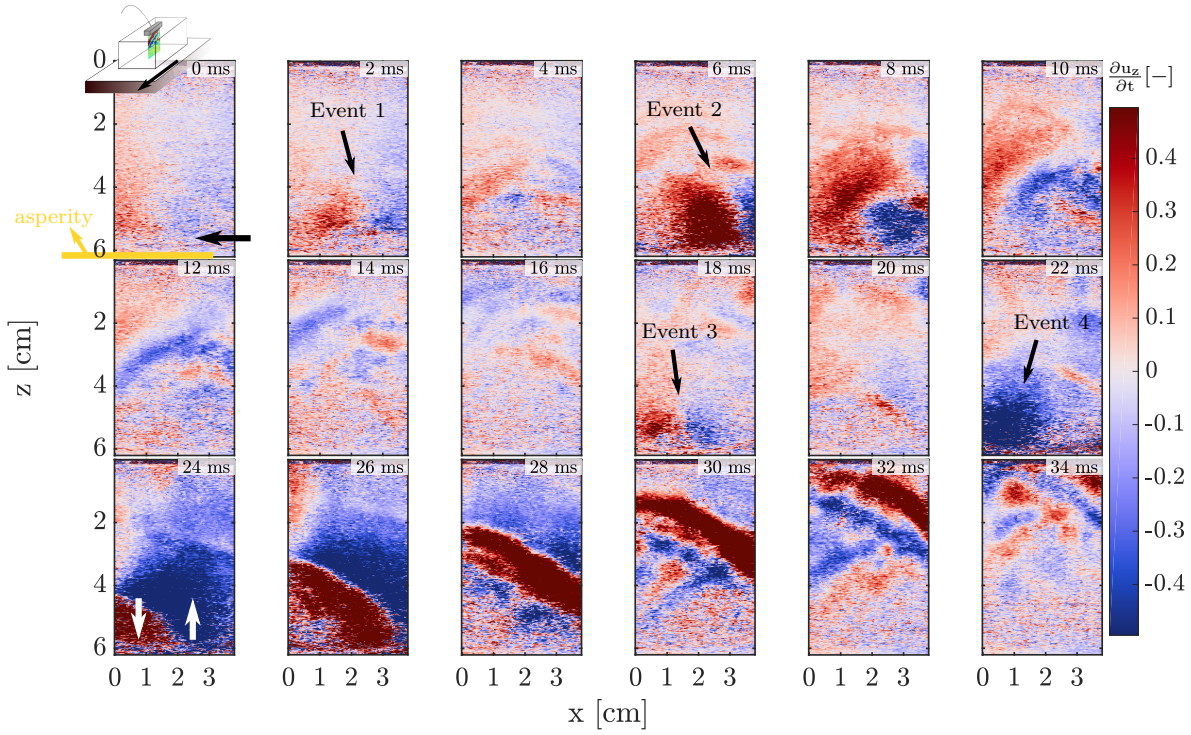


**Figure S2.** Particle velocity snapshots of a 34 ms long extract of the glass-hydrogel experiment (strong bi-material contrast). The direction of the plate movement is indicated by a black arrow in the first snapshot. The schematic experimental setup with the probe position is indicated by the inset in the same snapshot. Note that blue color denotes upwards polarization of the $z$-component of the particle velocity and red denotes downwards polarization of the $z$-component of the particle velocity. Event 3 corresponds to the localized event of figure Fig. 2 (main article) and event 4 to the rupture propagation across the whole asperity of Fig. 3 (main article)

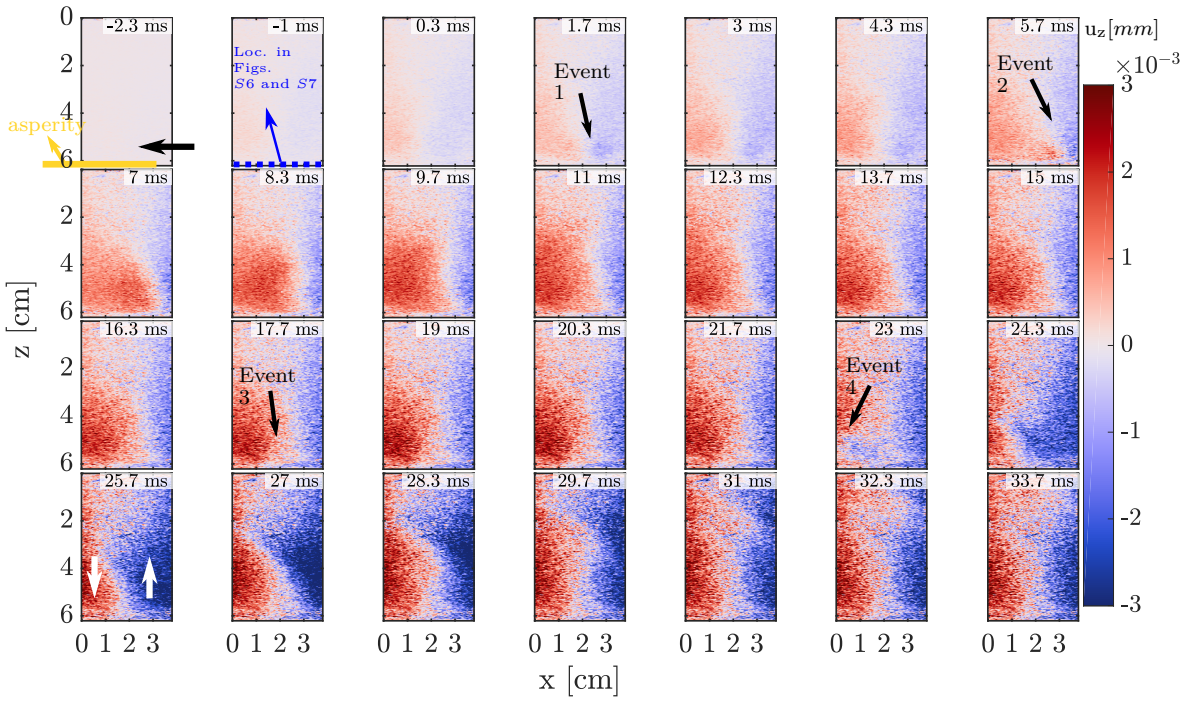


**Figure S3.** The cumulative displacement of the rupture cycle of Fig. S2 relative to −2.3 ms. The blue points in snapshot 2 indicate the approximate locations of the 1D displacement curves in Figs. S6 and S7. The three precursory events (1, 2 and 3) nucleate at the point of stress concentration, where the fault normal displacement changes sign. The supershear rupture however nucleates outside the imaging region and possibly not at a visible point of stress concentration. Note how the displacement field from 23 ms resembles a propagating slip pulse as computed by Andrews and Ben-Zion (1997).

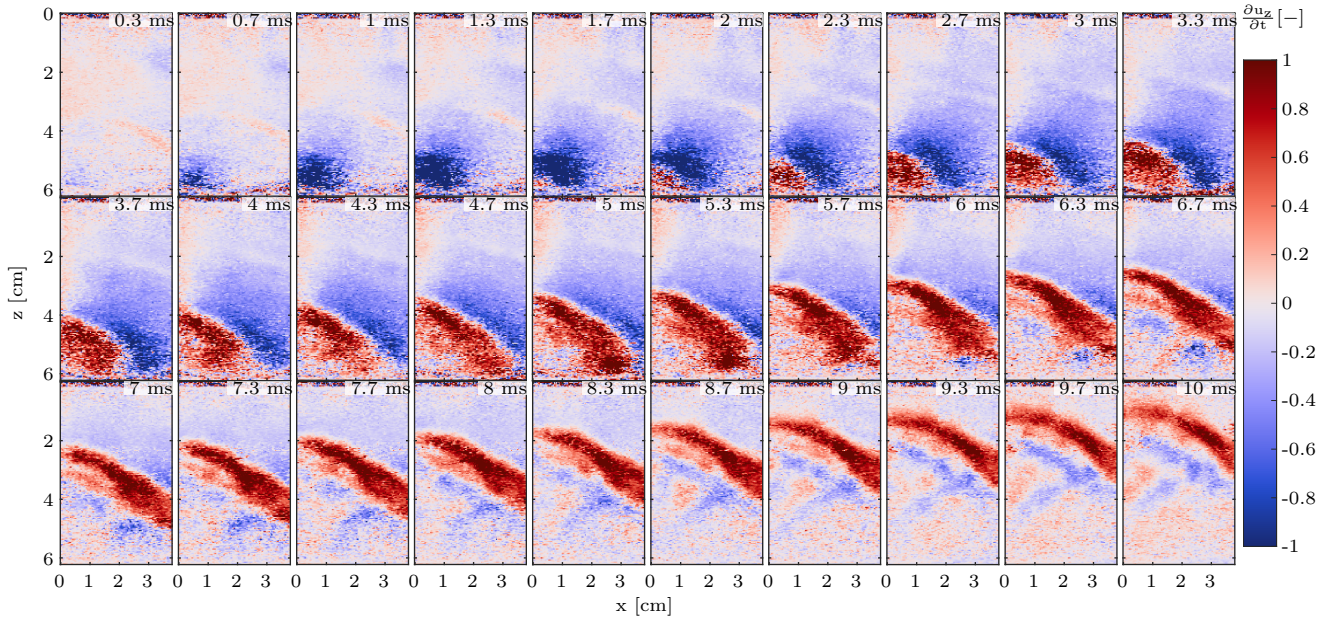


**Figure S4.** High temporal resolution particle velocity snapshots of the event in Fig. 3 (a) (main article). In contrast to Fig. 3 (a) (main article), the displayed snapshots are shown at the experimentally acquired temporal resolution.

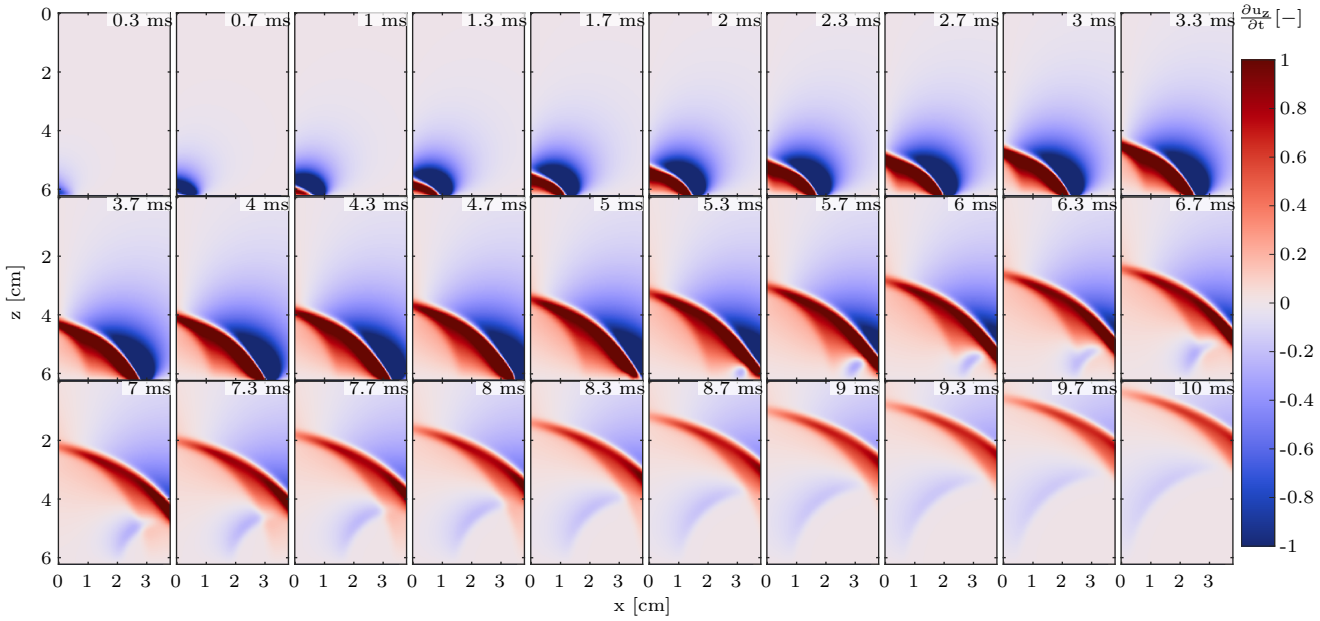


**Figure S5.** High temporal resolution particle velocity snapshots of the simulation in Fig. 3 (b) (main article). In contrast to Fig. 3 (a) and (b) (main article), the displayed snapshots are shown at the experimentally acquired temporal resolution.

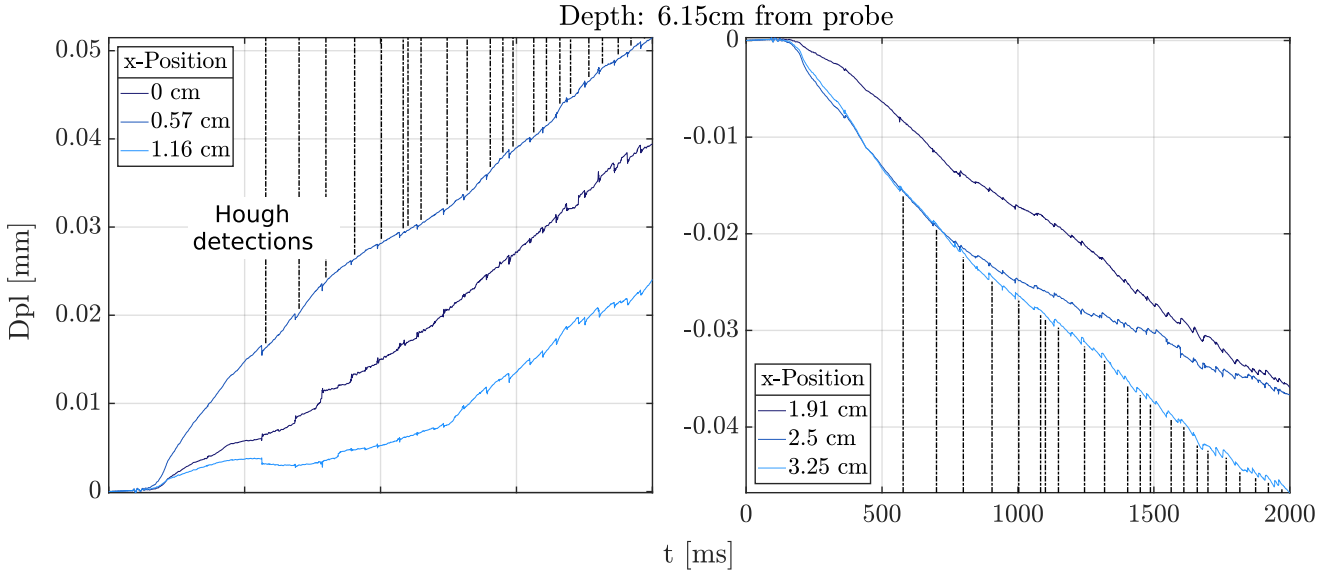


**Figure S6.** Displacement curves of the entire experimental time during the glass-hydrogel experiments for selected points on the rupture surface. Positive is downwards displacement, away from the probe as in Fig. S3. The overall trend is continuous deformation of the gel. The black dashed lines indicate successful supershear front detections by image segmentation and the Hough transform. Each sawtooth in the displacement curves thus represents a rupture as the one zoomed in on Fig. S7.

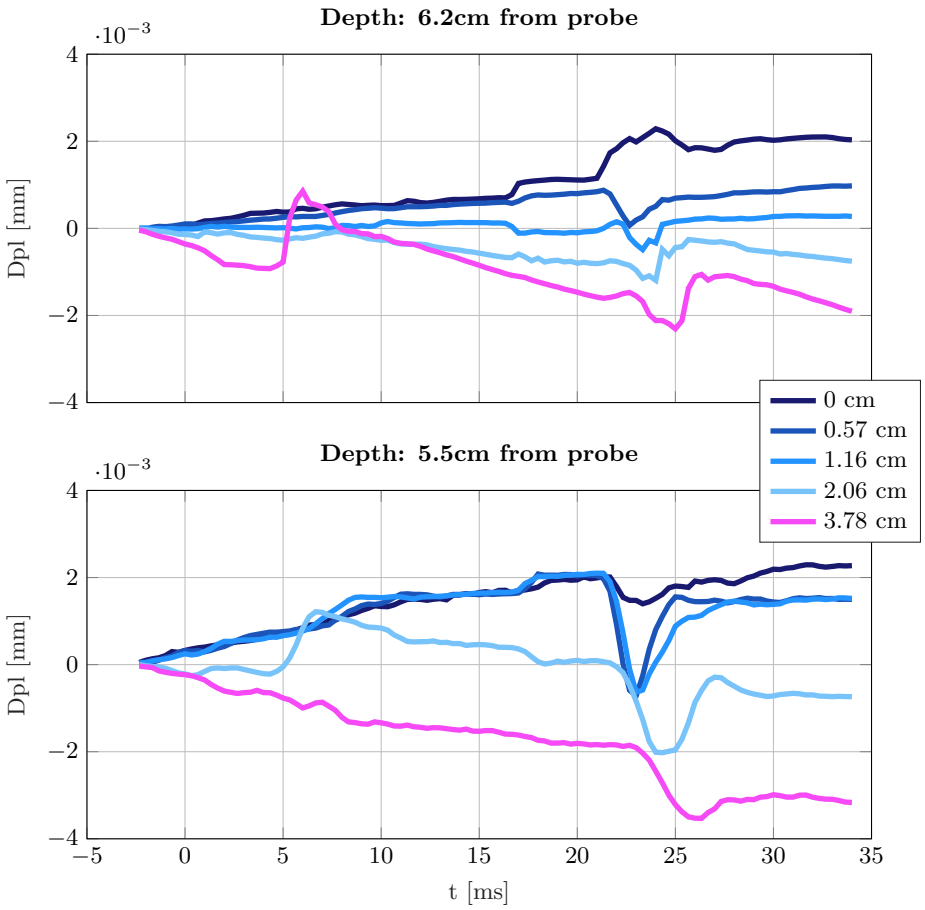


**Figure S7.** Cumulative $z$-displacement, calculated as the cumulative sum of the $z$-component of the measured particle velocity. All curves are taken at a specified $x$-location and plotted against time. Displacement against time for several points along $x$ on the rupture surface. The points are as close as possible to the fault, possibly partly inside the granular material. Positive is downwards displacement, away from the probe as in Fig. S3. The cycle from Fig. S3 is shown. In the displacement, the time-space evolution of the slip, whose dynamics are shown in Fig. S4, becomes evident. Note the event at x=2.06 cm x=3.78 cm and 6 ms. It represents Event 2 of Figs. S2 and S3.

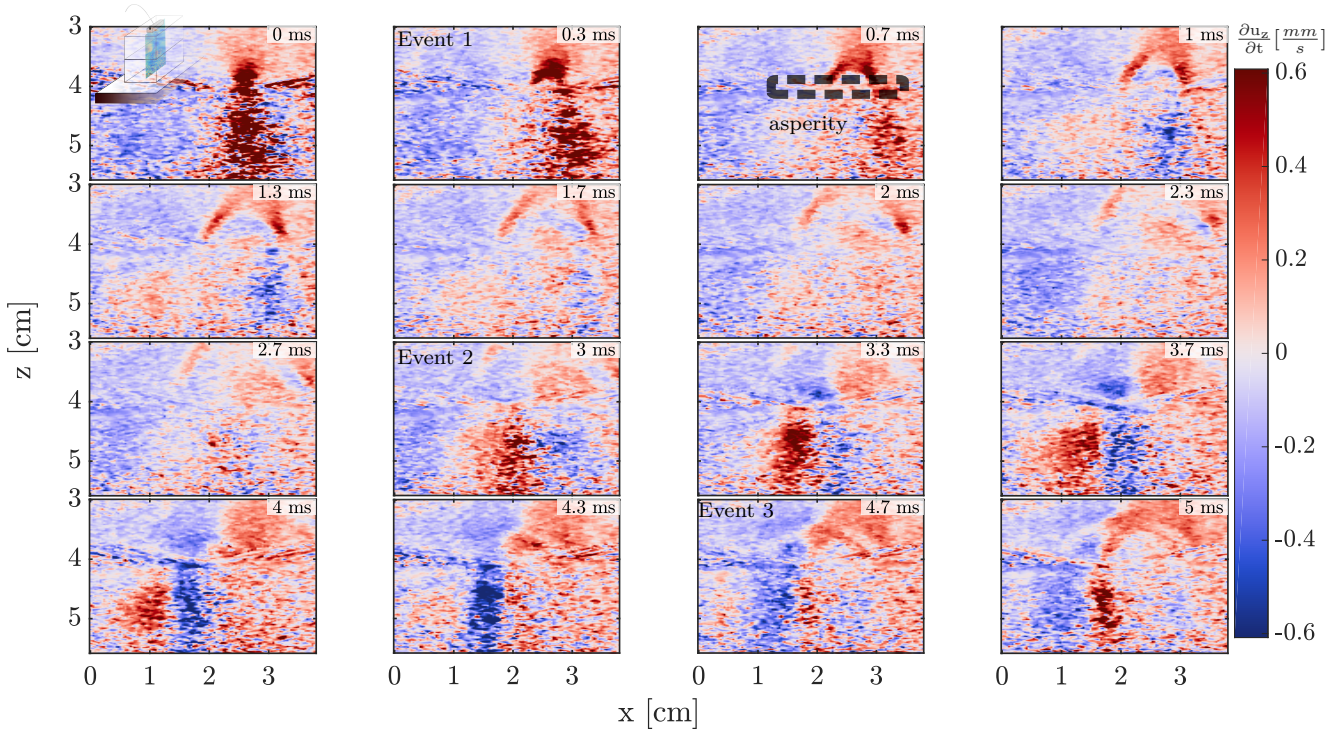


**Figure S8.** Particle velocity snapshots during an extract of the gel-gel rupture experiment (weak material contrast). Event 1 corresponds to the rupture propagation that is studied in Fig. 5 (main article) and event 2 to the localized event of figure Fig. 4 (main article).

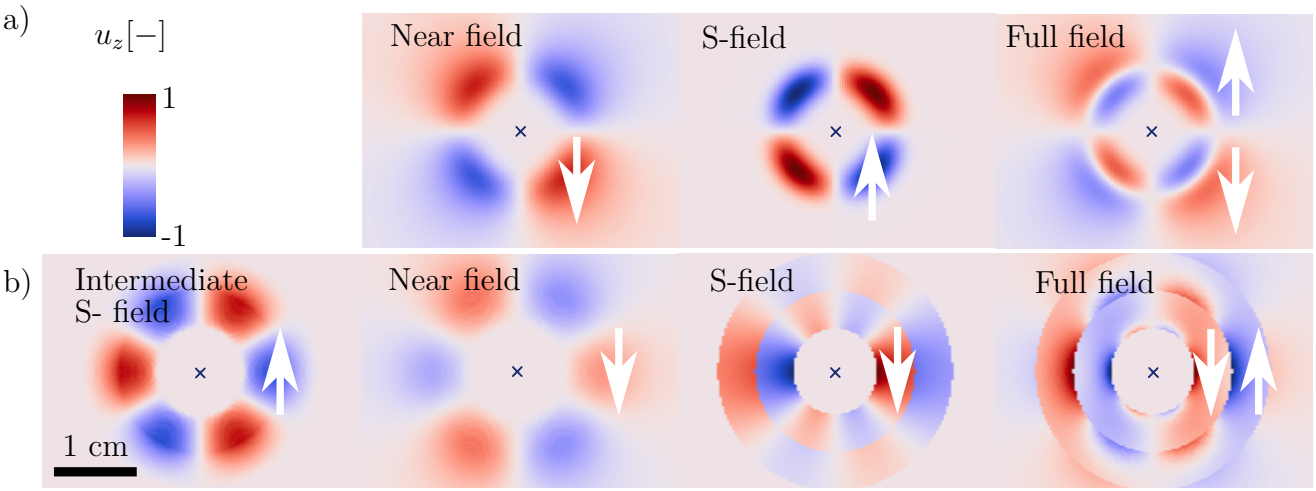


**Figure S9.** Radiation patterns for the $z-$component of the Green's functions for a right-pointing unidirectional shear force and a right-pointing double-couple. a) Displacement field of a point source resulting from the convolution of a Gaussian force in time with the Green's function of a unidirectional shear force (Eq. (5)). b) Particle velocity field of a point source resulting from the convolution of a ramp displacement in time with the Green's function of a double couple of forces (Eq. (6)).

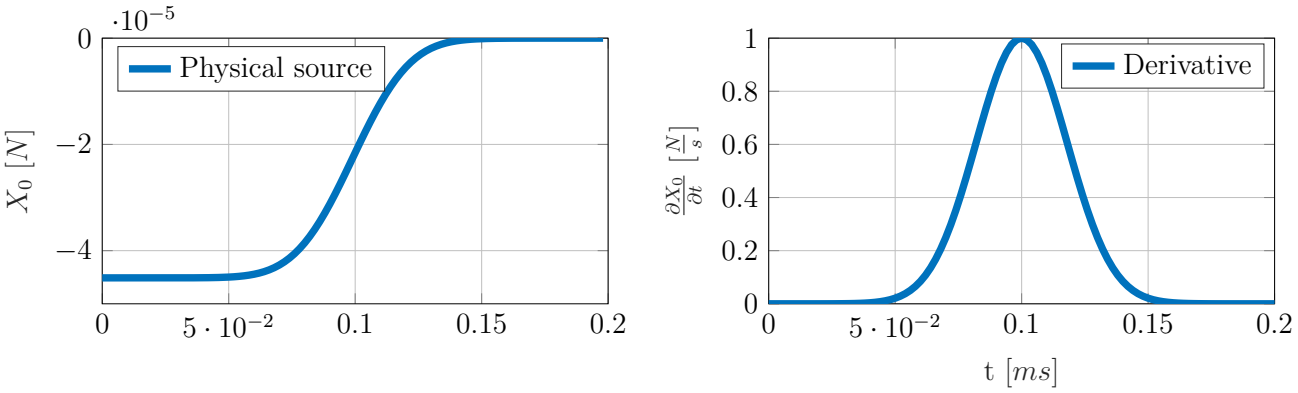


**Figure S10.** Source function for Fig. 2 (b) (main article).

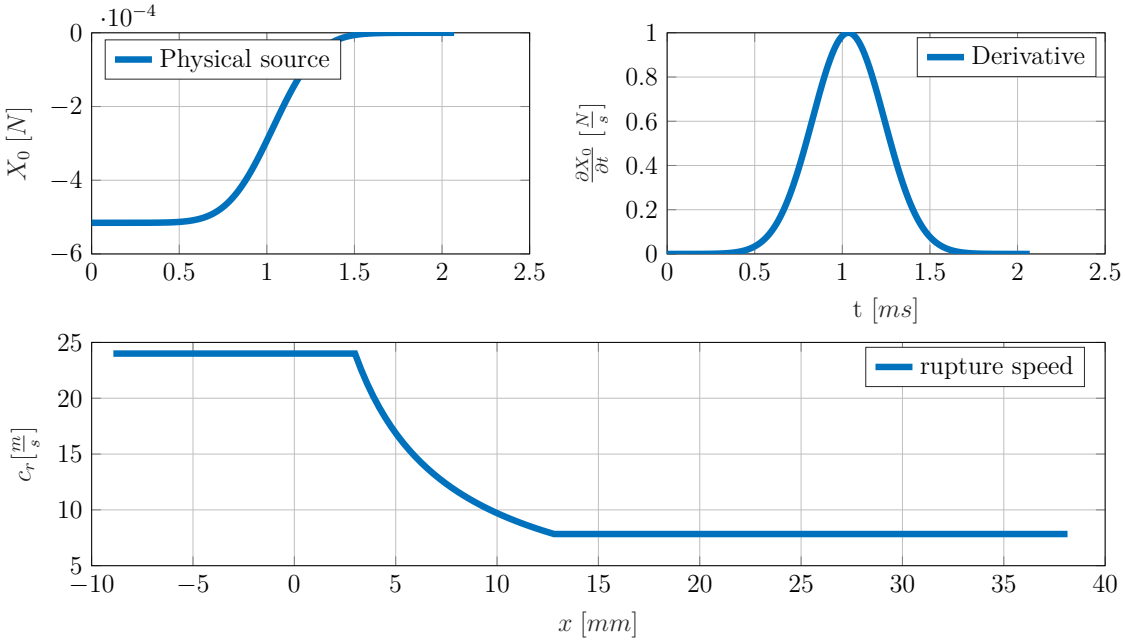


**Figure S11.** Top: Source function for Fig. 3 (b) (main article) and Fig. S5 (left) and its derivative (right). Bottom: Rupture speed profile in space. The rupture starts before the x-extension of the imaging plane.

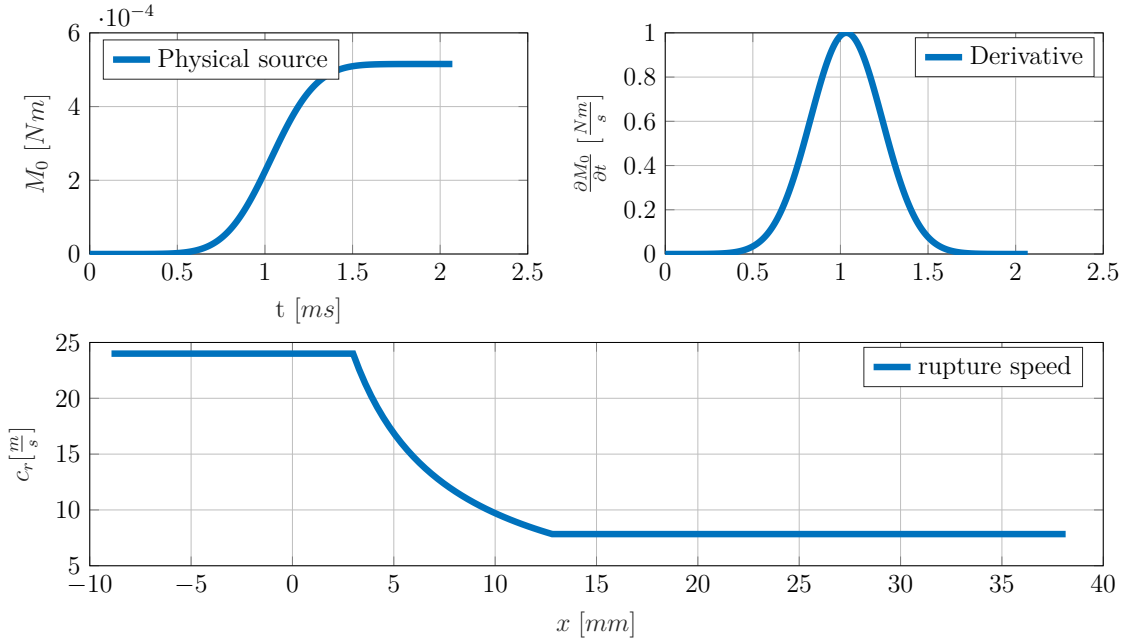


**Figure S12.** Source function for Fig. 3 (c) (main article) (left) and its derivative (right). Bottom: Rupture speed profile in space. The rupture starts before the x-extension of the imaging plane.

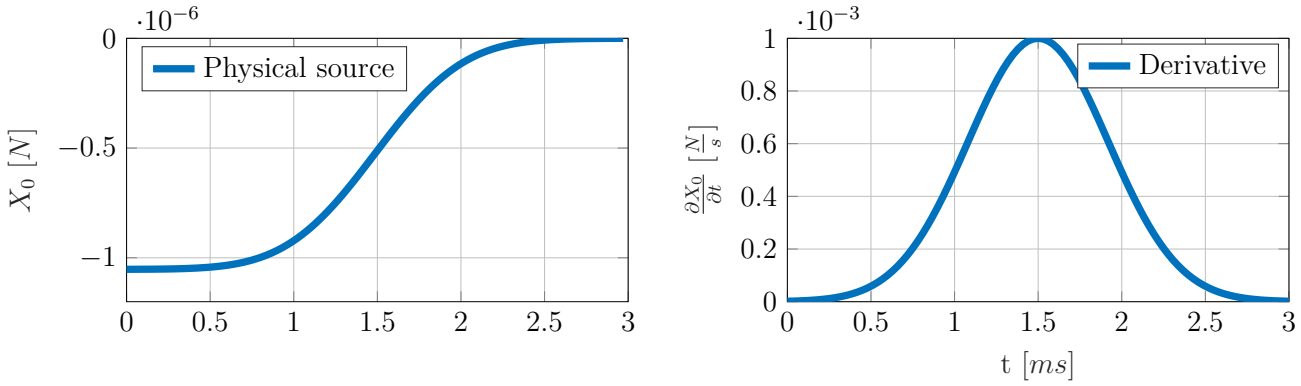


**Figure S13.** Source function for Fig. 4 (b) (main article).

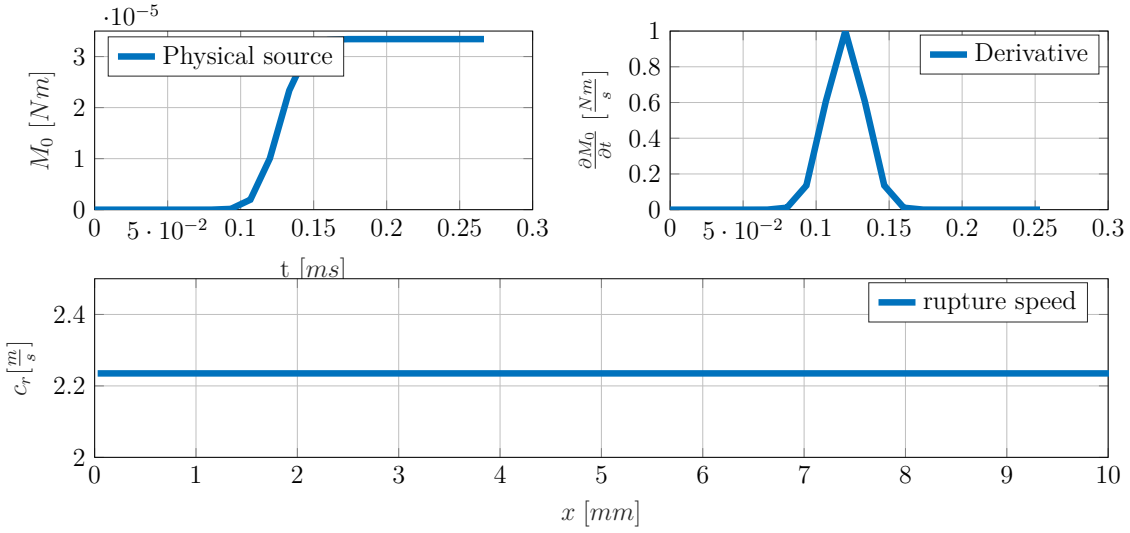


**Figure S14.** Source function for Fig. 5 (b) and (e)-(f) (main article).

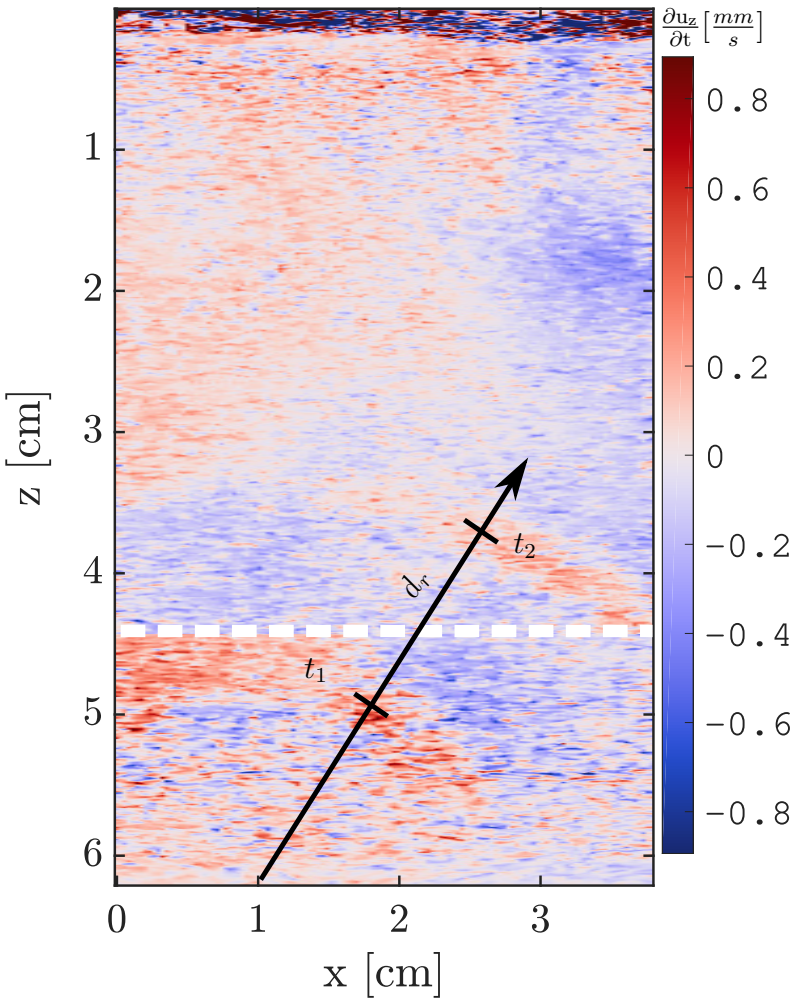


**Figure S15.** Shear wave time of flight on a composite image of two snapshots. The part below the white line shows a snapshot at $t_1$ and the upper part shows a snapshot at $t_2$. The shear wave speed is calculated from $v_s = \frac{dr}{t_2 - t_1}$ as $6.9 \pm 1\,\mathrm{m\,s^{-1}}$.

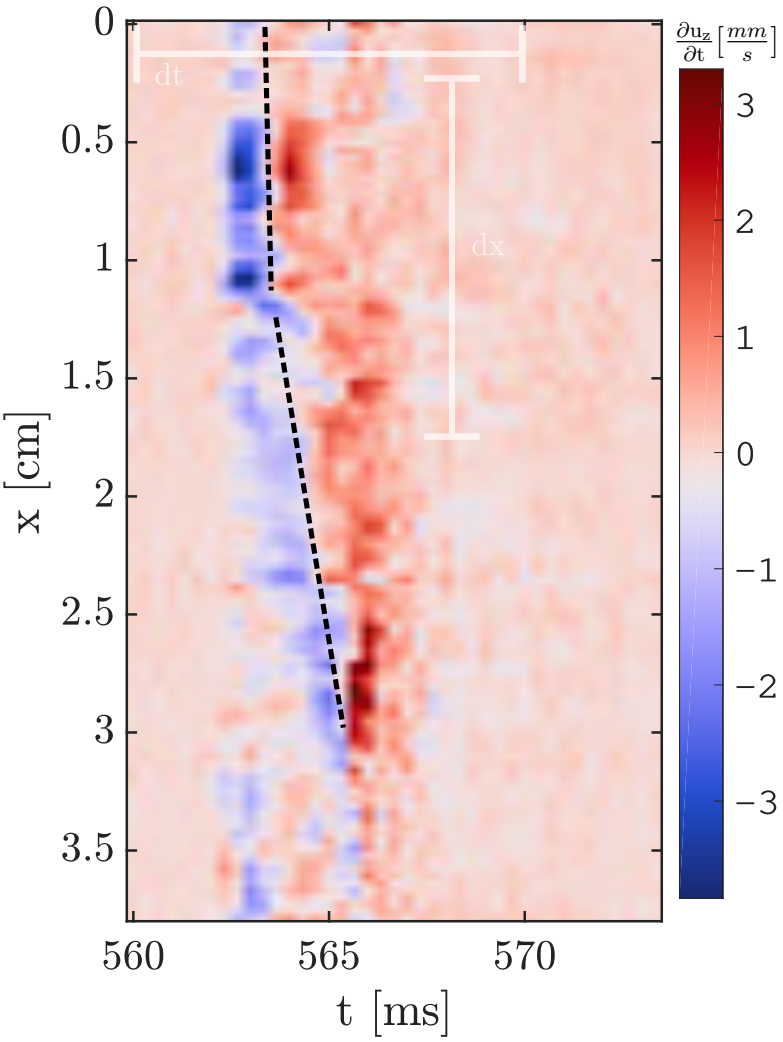


**Figure S16.** Example of the time of flight measurement of the rupture speed. The speed along the profile is not constant and the estimation by eye can only be tentative. The rupture speed equivalent to the black line on the indicated segment between 1.3 cm and 3 cm is calculated from: $v_r = \frac{dx}{t_2 - t_1}$, as $10.6 \pm 1\,\mathrm{m\,s^{-1}}$.

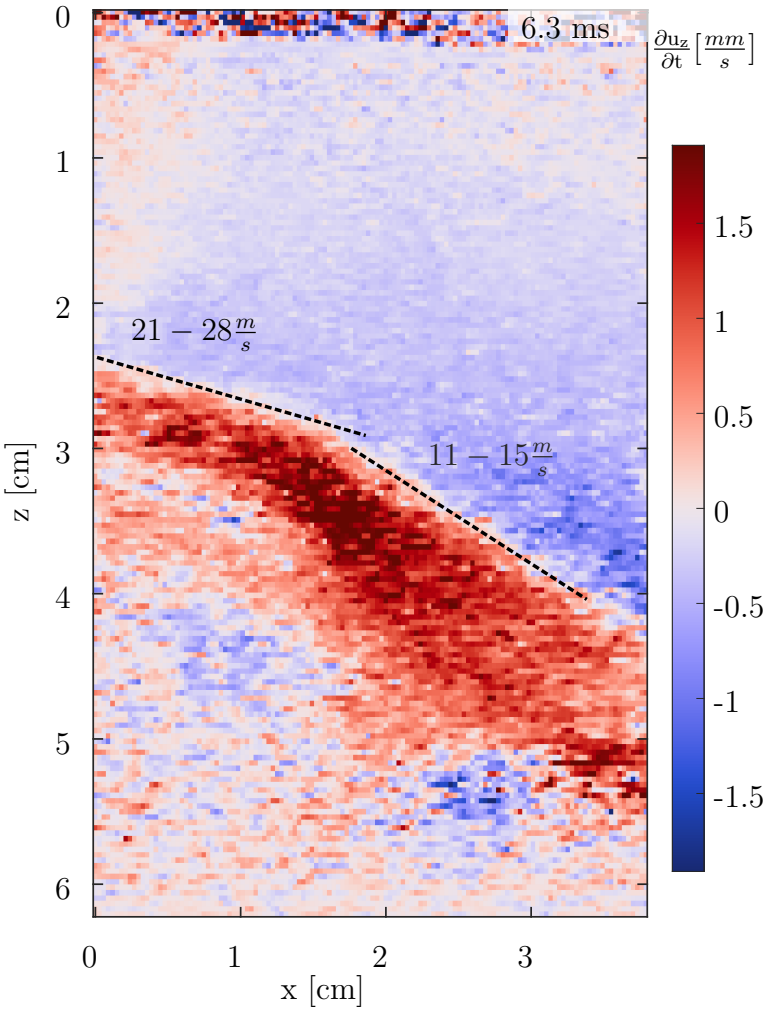


**Figure S17.** Example of the supershear front. Two slopes can clearly be identified, indicating a decelerating rupture. The rupture speed is calculated from the shear wave speed $c_s$ and the angle to the horizontal $\beta$: $v_r = \frac{c_s}{sin(\beta)}$. The rupture speed corresponding to each segment of the supershear fron is indicated.

## 5. Additional Supporting Information Captions (Files uploaded separately)

### 5.1. Caption for video S1

Wave propagation video of the particle velocities of the entire strong bi-material experiment. Blue color is upwards pointing and red color is downwards pointing particle velocity. The imaging plane is $x - z$ as described in the main article. Note how the main ruptures resemble each other indicating a stick-slip behaviour. The video extract corresponding to Figs. 2-3 of the main article can be found from 770 - 800 ms.

### 5.2. Caption for video S2

Wave propagation video of the particle velocities of the entire weak bimaterial experiment. Blue color is upwards pointing and red color is downwards pointing particle velocity. The imaging plane is $x - z$ as described in the main article. Here, both halfspace are imaged, albeit imaging quality is superior above the interface. The video extract corresponding to Figs. 4-5 of the main article starts at approximately 2396 ms.

## 6. References

## References

Aki, K., & Richards, P. G. (2009). Quantitative seismology. In *Book* (Second ed., p. 700). University Science Books.

Andrews, D. J., & Ben-Zion, Y. (1997). Wrinkle-like slip pulse on a fault between different materials. *Journal of Geophysical Research: Solid Earth*, *102*(B1), 553–571. doi: 10.1029/96JB02856

Pinton, G., Dahl, J., & Trahey, G. (2005, June). Rapid Tracking of Small Displacements with Ultrasound. In *IEEE Ultrasonics Symposium, 2005.* (Vol. 4, pp. 2062–2065). IEEE. doi: 10.1109/ULTSYM.2005.1603285

Sandrin, L., Catheline, S., Tanter, M., Hennequin, X., & Fink, M. (1999, October). Time-Resolved Pulsed Elastography with Ultrafast Ultrasonic Imaging. *Ultrasonic Imaging*, *21*(4), 259–272. doi: 10.1177/016173469902100402